Stiffness and fracture analysis of photovoltaic grade silicon plates

Lv Zhao[a], Anne Maynadier[a], Daniel Nelias[a,*]

[a] *Université de Lyon, INSA-Lyon, LaMCoS UMR CNRS 5259, F69621 Villeurbanne, FRANCE*

Abstract

The rigidity and the strength of photovoltaic cells, particularly the centerpiece-embedded silicon plates, are of great importance from an economical point of view since their reliability impacts the overall cost based on production, transportation and in-service use. The present work focuses on the solar-grade multi-crystalline silicon used in PV wafers. The aim is to characterize the Young's modulus and to analyze the fracture behavior at room temperature. The Si plates have been laser cut from two different manufacturing processes of silicon wafers, MCSi and RST. Due to the brittle behavior of Si at ambient temperature, 4-point bending tests have been performed. The beam hypothesis has been used to analyze bending tests for determining the Young's modulus. A correction strategy has then been proposed with a numerical model in order to determine with a higher accuracy the mechanical data and the measurement uncertainty. For fracture investigation, high speed imaging technique and fractography have been used to identify the failure mode as well as the crack origin. The Young's modulus is found to be 166±5 GPa for MCSi wafers. The anisotropic stiffness of RST plates is also revealed and correlates well with the micro-structural texture. Both kinds of plates fracture in trans-granular manner from the edges, where some defects are located due to laser cutting.

Keywords: Solar-grade multi-crystalline silicon, Photovoltaic cell, Young's modulus, Fracture, 4-point bending test, Finite Element analysis, High speed imaging, Fractography

*corresponding author: daniel.nelias@insa-lyon.fr

1. Introduction

In the photovoltaic (PV) domain most of the literature deals with the improvement of the electrical efficiency, by acting on some physico-chemical parameters. However, it is also important to address the material stiffness and the fracture behavior of the silicon wafers, since i) many silicon wafers break during the manufacturing process before the integration in PV cells and ii) post-manufacturing cracks created during transportation, installation or production can significantly decrease the efficiency of PV modules (Köntges et al., 2011; Paggi et al., 2014). Knowing that the fabrication cost of silicon wafers represents up to 40% of the total cost of a PV module (Möller et al., 2005), advanced manufacturing processes for thinner or more robust silicon wafers emerge increasingly. The characterization of the mechanical properties are of great practical interest, as the material's rigidity and fracture strength are highly influenced by the crystallinity and fabrication process (Popovich et al., 2011).

Crystalline silicon used in solar modules is of high purity. The silicon is a material whose mechanical properties depend on the temperature (Bourgeois et al., 1997; Masolin et al., 2012). It is, whether in the forms of single crystal or multi-crystal, a very brittle material at ambient temperature and it presents a brittle-ductile transition at temperature of about 600°C (Brede, 1993; Hull, 1999). Above this transition temperature, Si can undergo large plastic deformation due to dislocation movements, as discussed by Alexander and Haasen (1969).

Many investigations were carried out to characterize the stiffness of mono-crystalline silicon. Due to the cubic symmetry of the atom arrangements in the crystal lattice, the material owns only three independent parameters in the elastic stiffness tensor (Hull, 1999; Hopcroft et al., 2010; Masolin et al., 2012). The most accepted values were given by Hall (1967) from sound-velocity measurements. For multi-crystalline silicon, the rigidity depends on the distribution of crystallographic orientations of the grains. Indeed, a multi-crystalline silicon can be considered as an aggregate of multiple single grains separated by grain boundaries. If the average grain size is negligible compared to the dimensions of the studied structure, the multi-crystal can be homogenized into an isotropic material with only two parameters, the Young's modulus and the Poisson's ratio. The appropriate values of poly-crystalline silicon used for MEMS systems were reported by Sharpe Jr (2001) (E=160 GPa; ν=0.2). Funke et al. (2004) performed an analytical calculation over a representative volume element and gave E=162.5 GPa; ν=0.223 which were used for PV grade multi-crystalline silicon. However, these results should be used with caution for our application because the typical grain size is in centimeter range, which has almost the same order of magnitude as the specimen's dimension. Furthermore, if a specific texture exists, the characterization should account for the loading direction (bending axis here).

The silicon is brittle at room temperature. In the literature, most of the attention was paid to the fracture of single crystal. It is widely accepted that the cracks take place on the $\{111\}$ and $\{110\}$ crystallographic planes (Holland and Marder, 1998; Ebrahimi and Kalwani, 1999; Hauch et al., 1999; Pérez and Gumbsch, 2000; Sherman, 2009). Ebrahimi and Kalwani (1999) investigated the fracture toughness and the fracture path within a single crystalline silicon with Vickers micro-hardness indentation. Hauch et al. (1999); Li et al. (2005) reported the critical fracture energy of artificial pre-cracked silicon thick plates with an uni-axial tension apparatus. Many experimental investigations were based on 3 or 4-point bending tests (Sherman and Be'ery, 2003; Sherman, 2003, 2009), with the use of fractography to study the morphology of the crack surface. Regarding the multi-crystalline silicon, Brodie and Bahr (2003) investigated the influence of grain size on the fracture toughness. The results indicated that the latter has little dependence on the grain size when the typical size is over 30μm .

Whereas the improvement of the energetic efficiency of PV cells has captured since many years most of the efforts from the scientific community, mainly chemists and physicists, little is known about the thermo-mechanical strength and the fracture behavior of crystalline silicon plates, in itself or when embedded in a ready-for-use PV cell, under static or dynamic loading. In solar cell scale, Sander et al. (2013) investigated the crack pattern in encapsulated solar cells based on 4-point bending tests. Bending tests on flexible PV modules with initial cracks in silicon cells have also been performed in (Paggi et al., 2014). In that case, the role of fracture on the electric response was for the very first time monitored using the electroluminescence technique during the deformation process (for both monotonic and cyclic loading). Kaule et al.

(2014) studied the mechanical strength with different loading configurations relative to busbars. Kohler et al. (2014) performed photo- and electroluminescence analyses to locate defects such as material inhomogeneities or cracks. At the wafer scale, the former works concentrated mostly on the fracture stress with Weibull distribution in order to analyze the influencing factors. Funke et al. (2004) carried out biaxial tests to investigate the behavior of different kinds of wafers. Popovich et al. (2011) highlighted the effect of the crystallinity with 4-point bending tests. However, the fracture origin studies for multi-crystalline silicon wafer are rare to see. An interesting work was performed by Klute et al. (2014) who investigated the fracture origin for as-cut monocrystalline silicon wafers.

In this study, we are focusing on the mechanical strength of Si plates which stem from two different silicon wafer fabrication processes, i.e. classical sawing of multi-crystalline silicon produced by the ingot cast process (called MCSi) and Ribbon on Sacrificial Template process (called RST) (De Moro et al., 2012). The objective is to characterize the stiffness and to analyze the fracture behavior of these two kinds of plates at room temperature. 4-point bending tests were used for the overall study. Concerning the rigidity, we applied the beam theory to calculate the Young's modulus. A Finite Element (FE) model was carried out in order to analyze experimental data - with a correction procedure - and assess the overall rigidity with numerical simulations. Regarding the fracture behavior, high speed imaging technique and fractography were used to explore the fracture modes and sources.

The first part of the paper presents in details our samples, their fabrication and the induced micro-structures. A second part is dedicated to the experimental set up and presents the methods for the rigidity characterization and the fracture investigations. In the third part, the FE model is presented along with a correction strategy to better identify the Young's modulus from bending experiments. The fourth part presents the main results, followed by a discussion on the results and then the conclusion.

2. Presentation of the studied PV grade Silicon

2.1. Description of the specimens

As mentioned in the introduction, the specimens come from two kinds of manufacturing processes, MCSi and RST (detailled in section 2.1.1 and 2.1.2). Both kinds of plates are laser cut from silicon wafers to obtain the square shape of size 50×50mm^2. The RST plates are thinner (90μm thick) than the MCSi plates (170μm thick).

The following paragraphs detail the two different manufacturing processes and the induced micro-structures.

2.1.1. MCSi ingot cast

The MCSi manufacturing process is based on the solidification of melt silicon into ingot cast. As presented in Fig. 1, the crystal growth is controlled in a heated furnace where inert gas (argon) is injected in the crucible to guarantee an oxygen-free environment. After solidification, the ingot can be removed out of the furnace through the bottom opening. The ingot is then sawed into circular slices over the desired thickness. Wire sawing ensures good flatness and low roughness to the wafer. The latter is finally laser cut to get the final plate shape and size.

The characteristic grain shapes are presented in Fig. 2. Most grains are of a centimeter wide, that should be compared to the plate thickness (170μm for MCSi specimens). The grain boundaries are quite visible to the naked eye. It reveals that the grain shape is mostly polygonal with an aleatory distribution. In addition thin strips of twinning can be distinguished by light reflection contrast in many grains. They are parallel to each other in one grain but their orientation differs from one grain to another, which is a characteristic feature of grain disorientation.

2.1.2. RST crystal growth

RST manufacturing process aims to produce thinner silicon wafers in order to reduce the global cost of PV modules. As shown in Fig. 3, this kind of wafers is obtained by drawing a graphite ribbon through a crucible of molten silicon. The latter solidifies continuously on the two sides of the ribbon when it comes out of the crucible. A thin layer of pyrocarbon prevents the formation of Si-C precipitates during solidification at

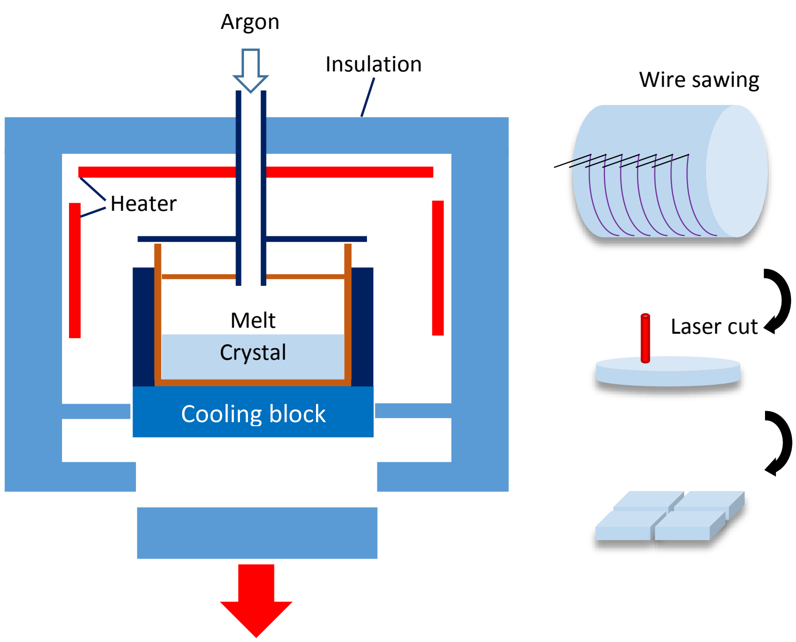

Figure 1: MCSi fabrication process

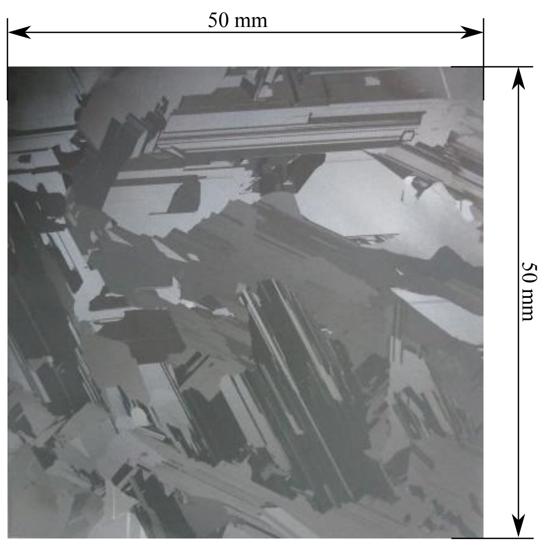

Figure 2: MCSi plate ($50{\times}50mm^2$)

the interface with the ribbon. Thus, a kind of ”sandwich” ribbon composed of silicon-carbon-silicon is formed. The layered ribbon is then laser cut, simultaneously on the two faces, in order to obtain the desired dimensions. In the following step, the carbon substrate is removed by heating the tri-plate above the carbon vaporization temperature. The obtained silicon layer is finally scoured to get the RST plate as shown in Fig. 4.

Due to the drawing effect, the grains have a predominant dimension in the drawing direction (often length greater than 50mm, width lower than 6mm, see Fig. 4). Even if the sample surface has an appearance of orange peel, one can easily observe that some grains have numerous twinning, covering the entire surface of the grain. The thickness of the produced silicon wafers depends of the drawing velocity, the considered ones have an average thickness of 90μm. Micro-graphs have shown that the thickness is not uniform along the plate edge and can vary locally in the range ±15% (see the thickness profiles in Appendix A.).

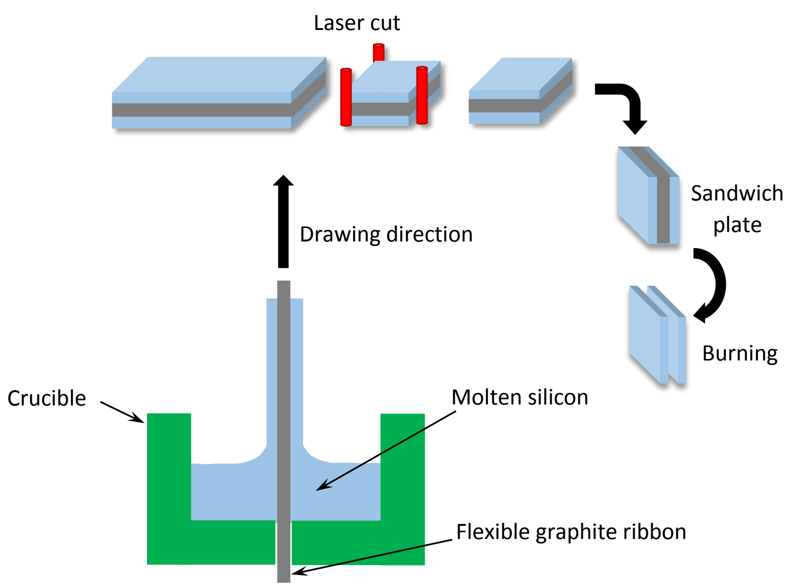

Figure 3: RST fabrication process

One can assume an inherent texture of the elongated grains with respect to the

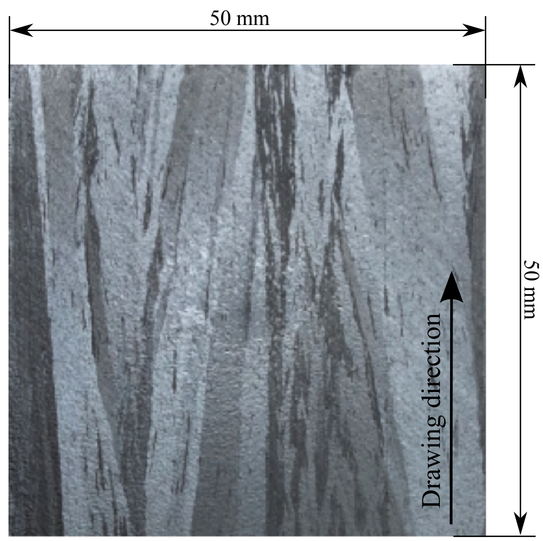

Figure 4: RST plate ($50\times50\text{mm}^2$)

drawing direction. Thus, EBSD measurements were performed to investigate the crystallographic orientations of the RST grains. The analyzed area was the central part of the plate surface that measures $5\times1\text{mm}^2$. An example of the EBSD color coded map and corresponding inverse pole figure are shown in Fig. 5. The color coded point clusters shown in the triangle next to the map represent the drawing direction (Y direction in the map) drawn in the crystallographic axis pole figures of all the studied grains. Thus, by looking at a green grain, it means that the drawing direction aligns with a [110] crystallographic direction of the grain since the green points are close to $\langle 101 \rangle$ pole. Interestingly, the green grains are quite dominant in the map, which signifies a crystallographic texture such that the [110] crystallographic direction of RST plates is primarily parallel to the drawing direction. Therefore two test configurations will be investigated, the first one when the bending axis is parallel to the grain orientation and second when it is perpendicular.

2.2. Expected material stiffness

For mono-crystalline silicon, due to the cubic symmetry of the crystal lattice, the stiffness tensor owns only 3 independent components C_{11}, C_{12}, and C_{44} in the crystallo-

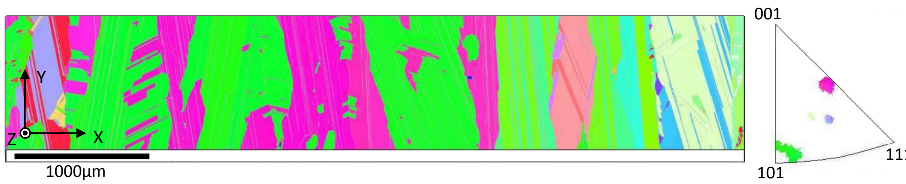

Figure 5: Color coded map (left) where Y corresponds to the drawing direction. Inverse pole figure (right),

graphic coordinate system of principal axes [100], [010], and [001]. At room temperature (298 K) and ambient pressure, the measurements that are considered as the most accurate in the literature were reported by Hall (1967), as recalled below:

$$\underline{\underline{C}} = \begin{pmatrix} 165.7 & 63.9 & 63.9 & & & \\ 63.9 & 165.7 & 63.9 & & & \\ 63.9 & 63.94 & 165.7 & & & \\ & & & 79.6 & & \\ & & & & 79.6 & \\ & & & & & 79.6 \end{pmatrix} (10^9 \, Pa)$$

A standard (100) silicon wafer owns three axes at [110], [−110], and [001]. The elastic properties can easily be inferred by a rotation of 45 degrees about the [001] axis:

$$\underline{\underline{C}} = \begin{pmatrix} 194.5 & 35.7 & 64.1 & & & \\ 35.7 & 194.5 & 64.1 & & & \\ 64.1 & 64.1 & 165.7 & & & \\ & & & 79.51 & & \\ & & & & 79.51 & \\ & & & & & 50.9 \end{pmatrix} (10^9 \, Pa)$$

It can be easily deduced that the smallest value of Young's modulus is 130 GPa (along the [100] directions) and the greatest is 188 GPa (along the [111] directions). In [110] directions, the rigidity measures 169 GPa. As an aggregate of multiple silicon single crystals, the multi-crystalline silicon owns theoretically an intermediate value of Young's modulus between 130 GPa and 188 GPa.

2.3. Preliminary discussion on the material fracture

The fracture of a multi-crystalline material, at the grain scale, may be trans-granular or inter-granular or both. In the literature regarding mono-crystalline silicon, the cleavage in some specific planes such as {111} and {110} was widely recognized as the fracture characteristic, not only in the framework of molecular dynamic simulations (Holland and Marder, 1998; Pérez and Gumbsch, 2000), but also experimentally (Hauch et al., 1999; Sherman and Be'ery, 2003; Sherman, 2003, 2009). However, for MCSi, different descriptions can be found. Coffman and James (2008) relied on the inter-granular cracks to investigate the grain boundary strength with molecular dynamic simulations. Conversely, (Chen and Qiao, 2007; Qiao and Chen, 2008) studied experimentally the grain boundary passage by cleavage crack in silicon film. Moreover, a recent publication (Infuso et al., 2014) considered both inter-granular and trans-granular cracking in their failure simulation with cohesive zone method for MCSi solar cells. Due to the complex atomic arrangement at a grain boundary which involves both twist and tilt angles, the surface energy is hardly accurately assessed by simulations whereas experimental data have not been published yet, to the authors' knowledge. However, the identification of the failure mode is an interesting issue since that helps to understand the fracture mechanisms, may give some ideas to reduce failure during manufacturing, and can guide designers to optimize encapsulated PV cells in order to be more reliable.

The failure initiates mostly from defects such as impurities and pre-existing cracks that act as local stress risers. For solar grade silicon, the strength should be free of size effect, as the grains are in centimeter range which exceeds the size effect threshold of 30 μm reported by Brodie and Bahr (2003). It has been mentioned in the literature that the strength of mono-crystalline silicon without pre-crack ranges between 5 and 7 GPa (Kozhushko et al., 2007), which is much higher than that of MCSi wafers which barely reaches 1 GPa. The commonly recognized fracture cause are subsurface micro-cracks generated by wire sawing, as discussed by Möller et al. (2005); Wu and Melkote (2013) and spotted in Klute et al. (2014). Inclusions can also be critical fracture origins, as Si-C particles are frequently found in silicon ingots. These particles have sharp edges, and may be very large – up to 50μm or even more (Søiland et al., 2004). Moreover, other defects induced by alternative cutting processes, such as the laser cutting, are less studied. Sudani et al. (2009) investigated the wafer strength for different cutting parameters like repetition rate and pulse width.

With respect to the manufacturing processes of our silicon wafers, the potential defects would be the micro-cracks present at the near surface due to wire-sawing (for MCSi plates), the inclusions generated in the bulk during the solidification (for both kinds), and the laser cutting induced defects at the edges (for both kinds). In addition, it should be noted that the RST plates locally undergo important variations of thickness, that may also induce local over-stress during loading.

3. Experimental methods

3.1. Characterization with 4-point bending tests

Since the studied material is brittle at room temperature and the thickness of the specimen is small, tensile tests are very difficult to perform. Conversely, bending tests are very appropriate for thin specimens and therefore have been often used in the literature for thin silicon specimens (Samuels and Roberts, 1989; Popovich et al., 2011; Klute et al., 2014). Moreover, the Young's modulus and the fracture stress can be easily calculated from the force-deflection relationship by beam theory.

In this study, a 4-point bending test bench – as shown schematically in Fig. 6 – has been preferred to 3-point bending configuration in order to have a large area of uniform mechanical state, which is in accordance with the recommendation in ASTM C 1161-02c. Indeed, between the two central contact lines, the radius of curvature of the deformed plate is constant - and so the stress varies only with the distance from the central plane - and the influence of the micro-structure on the fracture can be more easily observed. In Fig. 6, P represents the punch load force, a and d indicate the inner and outer spans, δ stands for the load cell displacement, which is also the plate deflection under the punch rollers. The parameters of our experimental set up are given in Table 1. The outer and inner spans correlate well with the recommendations in ASTM C 1161-02c, while the suggestion for the punch roller radius (approximately 1.5 times the specimen thickness) is not practical in our case. The punch and support

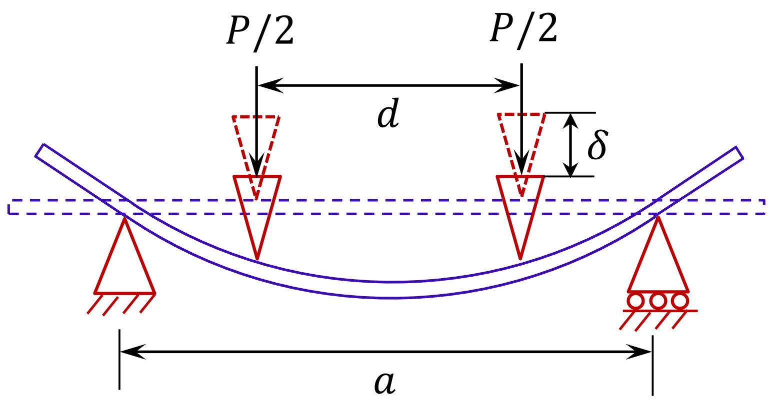

Figure 6: 4-point bending test

rollers are in steel, and of low roughness to avoid local stress concentration at the contact interfaces.

The tests were performed at constant punch velocity with a LLOYD-Ametek LF-PLUS electro-mechanical machine. The cross-head moving down rate was 0.2mm/min, which means a strain rate in the order of $10^{-6}s^{-1}$ and thus a quasi-static loading. An integrated displacement sensor provided in real time the punch displacement, and an external force sensor with a capacity of 10N measured the reaction force on the punch. Thus, a force-deflection (P ; δ) curve could be drawn after each test.

Table 1: Parameters of experimental set up

Outer span	**Inner span**	**Punch roller radius**
a=21mm	d=40mm	r=3mm

The expressions for the maximum tensile strain and stress in function of the load force, the deflection, the plate dimensions and contact spans were given by Bruneau and Pratt (1962) as listed below:

$$\varepsilon_{max} = \frac{6h\delta}{(a-d)(a+2d)} \tag{1}$$

$$\sigma_{max} = \frac{3P(a-d)}{2bh^2} \tag{2}$$

where b denotes the width of the specimen along the transverse direction and h the thickness.

It yields for the Young's modulus:

$$E = \frac{P(a-d)^2(a+2d)}{4bh^3\delta} \tag{3}$$

Our characterization work was based on Eq. 3. It should be noted that the beam theory is simplistic and neglects the Poisson's effect. It relies on the assumption that the material is homogeneous and isotropic. Moreover, the contact is assumed to be perfect and invariant. Thus, the results given by Eq. 3 should be used with caution. To ensure the validity of our measurements and correct them if necessary, a FE model was elaborated and parametric simulations were performed, which will be addressed in Section 4.

For the MCSi plates, as the grain morphology is quite aleatory (see Section 2.1.1), one may assume that the wafer orientation does not have any influence on the Young's modulus (average). Due to the manufacturing process, the RST plates have elongated grains along the drawing direction (see Fig. 4), and preliminary EBSD measurements revealed a texture (see Fig. 5). Thus, directional characterization was taken into account by considering the Young's modulus along the drawing direction different from the one along the perpendicular direction.

3.2. Fracture investigations with high speed imaging and fractography

3.2.1. Fracture mode analysis

The crack propagation velocity in a silicon mono-crystal was reported as $2,300 \pm 300$m.s^{-1} and 3,300m.s^{-1} by Hauch et al. (1999) and Sherman and Be'ery (2003), respectively. For solar grade silicon plates, as the grains are visible to the naked eye, it is easy to determine the failure mode in experiments, as long as the crack pattern can be captured by an imaging device. Thus, in our 4-point bending framework, a high speed imaging technique was used in order to track the cracking process. Since it was impossible to set up the high speed camera below the plate, a tilted mirror (with 45 deg inclination from the plate surface) was put between the two outer supports (cylinders). The view of the camera that was horizontally placed is presented in Fig. 7. It should be noted that due to the span of the support, the width of the mirror is smaller than that of the plate. This leaded to a reduced view of the plate surface, but the area of interest, i.e. the zone in uniform tension between the two punch rollers, could still be observed.

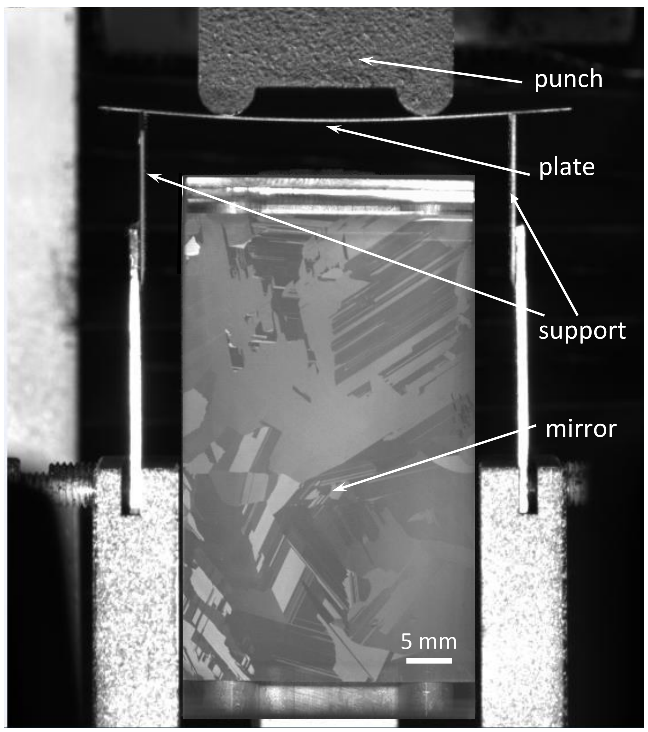

Figure 7: 4-point bending with mirror.

The camera used in this study is a Phantom V710 one, which is adjustable in frequency and resolution, with one feature wanes when the other one waxes. The maximum frequency at which the resolution allowed to clearly cover the mirror surface was 33,000Hz. In the present analysis, the frequency of the camera was fixed at 13,000Hz to obtain images of good quality for further digital treatment which consisted of subtraction of two consecutive images. Note that the high speed camera was manually triggered to record the 2s preceding the cracking, once the first noise was heard by the operator.

3.2.2. Fracture origin identification

Considering the reported crack propagation velocity, during the time increment between two successive photos, a crack could travel about 75mm over the maximum frequency i.e. 33,000Hz, yet the plate length is only 50mm. It means that the high speed camera used here has little chance to capture the propagation of the crack. However, this high speed imaging set-up was used to identify the first cracks. Knowing that the fracture origin is usually surrounded by some special surface marks, a fractographic investigation was then carried out only for the first crack(s) in order to find out the defect that initiated the cracking. In this work, a Keyence confocal microscope (VHX-2000) was used to draw the crack surface micrographs.

Under bending solicitation, the crack profile presents a quarter of an ellipse followed by a straight line representing the crack front in the thickness of the plate (Frechette, 1990). This feature is shown schematically in Fig. 8, inspired from the works of Frechette (1990) and Sherman (2009). When the crack front encounters severe surface toughness, some elastic waves are released. The latter interact with the advancing crack front and then generate the so called Wallner lines (Fig. 8). Particularly, in Sherman and Be'ery (2003); Sherman (2003, 2009), the authors reported specific surface perturbations in the {111} cleavage planes, which have also been found in our preliminary tests on mono-crystalline silicon plates. A typical fractography image is shown in Fig. 9, exhibiting corrugated instabilities near the compression side (top), the form of terrace-like kink instabilities near the tensile side as well as the imaginary crack front profile. The above described Wallner lines and specific surface perturbations allow to determine the crack propagation direction. Thus, they were used in this study to localize the fracture origin where one could observe two opposite propagation directions. Particularly, the specific surface perturbations allowed to identify the crack plane nature as {111} planes.

3.2.3. Weibull distribution analysis

Weibull distribution (Weibull, 1951) is widely used in fracture strength characterization for brittle materials, as recommended in ASTM C 1161-02c. The distribution involves the identification of two parameters i.e. the characteristic fracture stress σ_θ and the slope or modulus m that highlight the characteristic size of defects at the origin of failure and the scatter of the defect sizes due to the manufacturing process. A Weibull analysis was performed in order to better understand the correlation between the mechanical strength and the identified fracture origin, the later being mostly linked to the manufacturing process used. The fracture stresses were calculated with Eq. 2 for MCSi plates and RST plates (in the two loading configurations for the later).

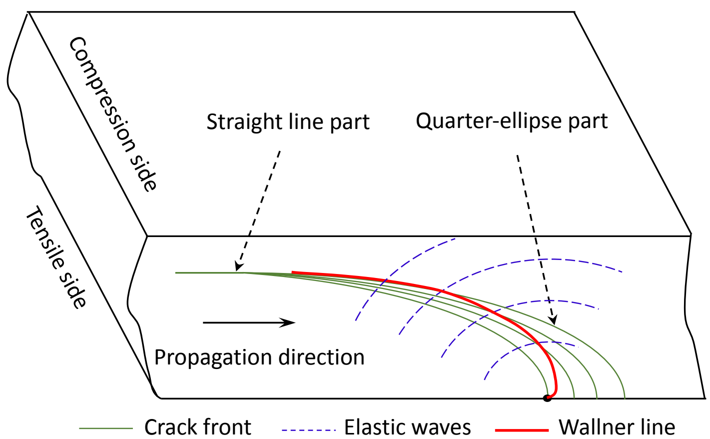

Figure 8: Crack profile scheme under bending with Wallner lines

4. FE analysis of the 4-point bending test

A parametric finite element model was elaborated using the commercial FE package Abaqus V6.13 in order to reproduce more faithfully the bending tests. As shown in Figs. 10 and 11, the microstructure of the material could be taken into account. Three configurations were considered, one for MCSi and two for RST depending on the grain orientations that could be either longitudinal or transverse. For the MCSi micro-structure, the grain boundaries were determined with 2D Voronoi tessellation

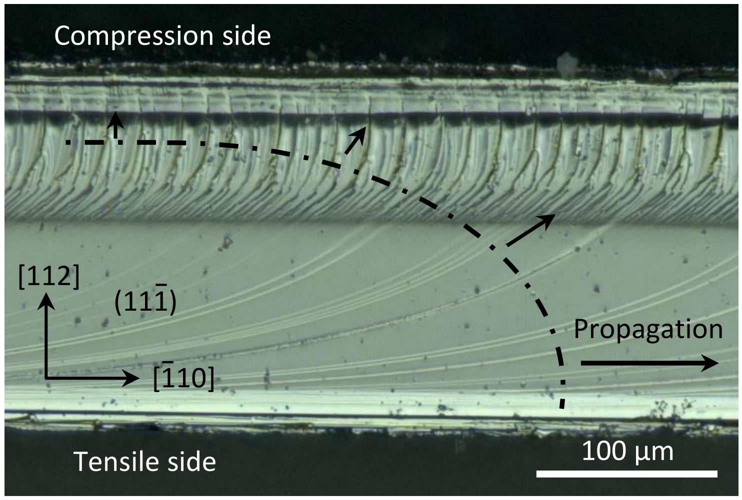

Figure 9: Optical image of the $(11\bar{1})$ fracture surface of mono-crystalline silicon under bending.

assuming that the modeled grains in the MCSi plates have aleatory polygonal shapes and that they have more or less the same characteristic size (see Fig. 2). The grain determination is performed as following: firstly, a set of points were obtained at the centers of the squares that equally partitioned the plate surface, then a moderate random deviation (between 0 and 40% of the square length) was applied to each point to get the Voronoi seeds, finally the plate surface was partitioned into the Voronoi cells with these seeds. For the RST plates, the grains were modeled by an assembly of adjacent rectangles of same width, which were representative for the real grain shapes (see Fig. 4). To have a parametric numerical set up, a Matlab code was developed and coupled to the Abaqus script, so that the plate thickness, the grain shape and orientation could be easily modified. Thus, many numerical simulations were carried out to evaluate the influence of each parameter.

Quadratic triangular continuum shell elements with 6 nodes (SC6R) have been used to mesh the plate. This family of elements was considered suitable for our application since the continuum shell wedge performs very well in bending and permits to ensure a uniform mesh. The element size was such that the plate edge was covered by about 150 elements with 4 layers of elements in the thickness. The material orientations associated to these elements, which are also the crystallographic orientations, could be

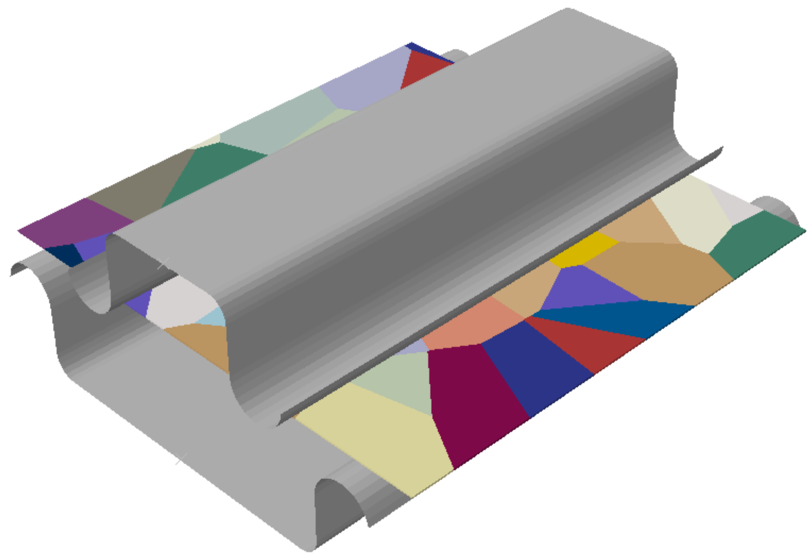

Figure 10: Example of 4-point bending FE model for a MCSi plate

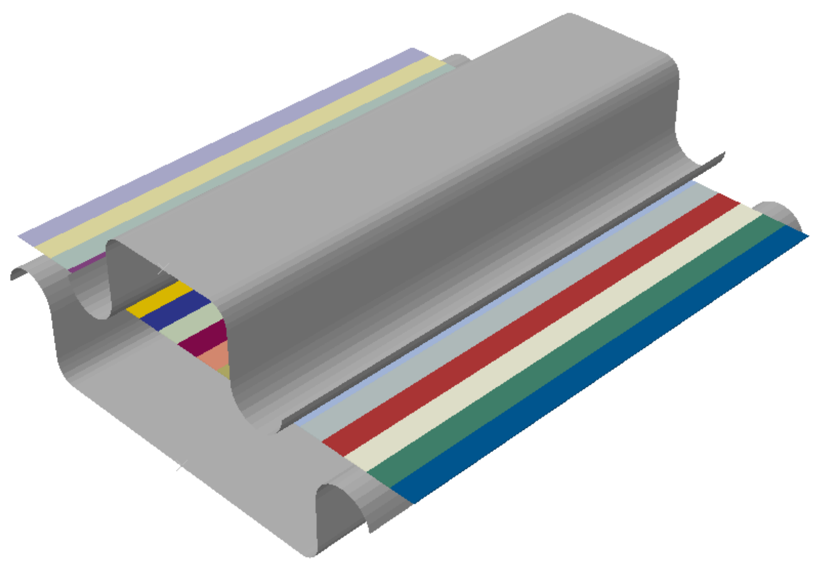

Figure 11: Example of 4-point bending FE model for a RST plate

chosen in a random manner or associated with a micro-structural texture. In this numerical study, none of locking pathologies has been encountered, with respect to a well refined mesh and a moderate flexural deflection applied in the simulations. For a future development, the authors might suggest the use of solid shell finite elements with EAS and ANS techniques. They are indeed required to model the solar cell plate embedded in PV modules (Paggi et al., 2016) or for solar cells bonded to substrates for flexible electronics (Reinoso et al., 2016). In those applications, large displacements occur due to the much higher flexibility of the system caused by the surrounding polymer.

4.1. Model validation

As a first step, a plate cut from the standard PV wafer along the cleavage planes (110) was considered. The crystallographic directions with respect to the plate structure are shown in Fig. 12. This plate was tested experimentally and simulated thanks to the FE model. The elastic properties of the plate corresponded to the second elastic stiffness tensor presented in Section 2.2. A friction coefficient of 0.15 was used at the interfaces between the plate and the rollers (Yang et al., 2008). Figure 13 presents the force-deflection curves for a 193μm thick plate obtained by FE simulation (red plain line) and experiment (blue dotted line). The excellent agreement found here for the mono-crystal Si specimen permits to validate both the model and the experimental procedure.

4.2. Correction of the analytical solution based on the beam theory

In a second stage, some preliminary calculations were performed in order to assess the relative error due to the identification of the Young's modulus using the beam theory i.e. when neglecting the Poisson's effect and the contact interactions. A bending simulation for a homogeneous isotropic plate with a Young's modulus of 160 GPa and a Poisson's ratio of 0.2 was performed. The plate thickness was chosen at 175 μm. The numerical force-deflection curve in the range $[0.1 - 0.3]$ mm was extracted to assess the Young's modulus derived from Eq. 3. The calculated value is 174.4 GPa, which points out an overestimation of 9% in the experimental characterization when the analytical calculation by Eq. 3 is used.

The advantage for extracting a deflection interval rather than a force one is that the relative error remains almost the same for a large range of plate thickness, as presented

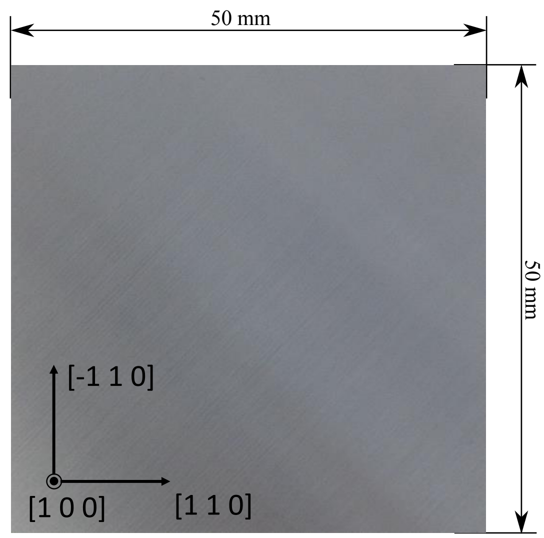

Figure 12: Silicon plate made from a single Si crystal

in Fig. 14. This finding is of great interest since the RST plates are much thinner than the MCSi plates and for both kinds, the thicknesses of the plates can differ from one to another. When this correction strategy was applied on the experimental curve in Fig. 13, the deduced Young's modulus was 170 GPa, which was extremely close to the theoretical value of 169 GPa.

The friction coefficient used initially was 0.15. In order to assess the influence of the friction coefficient on the simulation results, we varied this parameter from 0.1 to 0.3 with an increment of 0.025. The range [0.1 – 0.3] was also used in the simulations of (Funke et al., 2004). The thickness and the material properties of the plate were the same as in the previous paragraph. From Fig. 15, it can be noticed that the friction coefficient has a small effect on the relative error, with a relative error ranging from 8.5 to 10%. Therefore, the relative error of 9% will be used later for correction of the experimental characterization.

4.3. Numerical characterization of Young's modulus

Finally, several parametric studies were carried out for heterogeneous Si plates in order to assess the equivalent Young's modulus from a numerical point of view. For

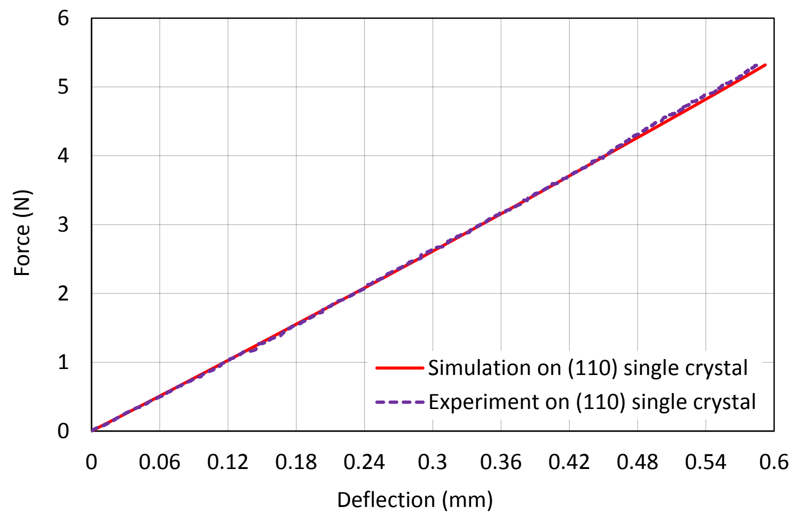

Figure 13: Comparaison of numerical and experimental force-deflection curves on a 193 µm thick monocrystalline wafer under 4-point bending

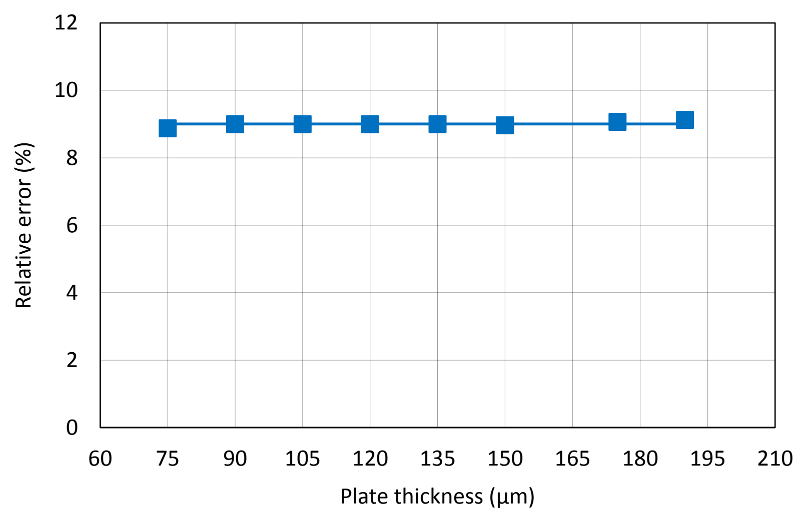

Figure 14: Influence of the plate thicknesses over the relative error based on [0.1 − 0.3] mm deflection interval for stiffness calculation. The straight line denotes the mean value of the assessed relative errors.

MCSi kind, the plate contained 49 grains (see Fig. 10), which is representative of a real plate (see Fig. 2), when the twins are not considered. For RST kind, the plate

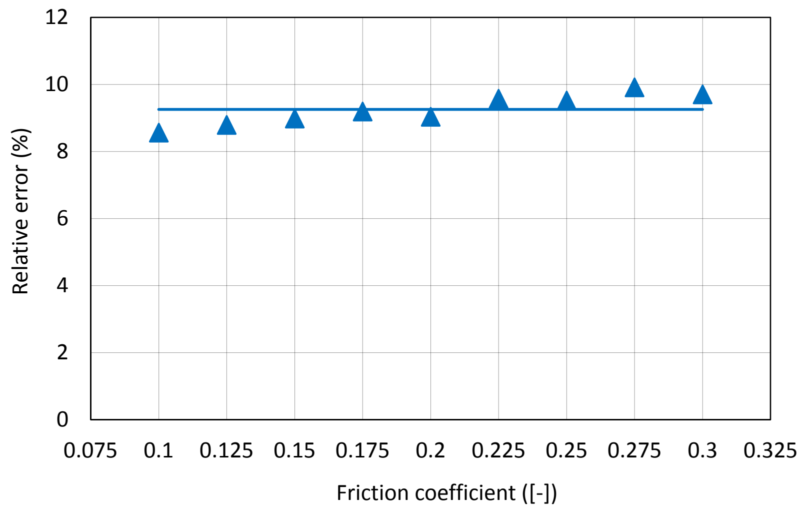

Figure 15: Influence of the friction coefficient over the relative error based on [0.1 – 0.3] mm deflection interval for stiffness calculation. The straight line denotes the mean value of the assessed relative errors.

contained 20 rectangular grains (see Fig. 11), which also corresponded to the typical specimen (see Fig. 4). The simulations were performed with the same grain geometry and distribution but with different grain orientations. Regarding the orientation determination, aleatory distribution was selected for MCSi kind. However, artificial texture compatible with the EBSD measurements was considered for RST kind, that is the [110] directions of the grains are parallel to the drawing direction (see Section 2.1.2). As one can notice in Fig. 5, about 70% of the grains are affected by this texture. This particular orientation distribution for FE model was achieved with a Matlab code. It firstly consisted in finding out all the possible Euler angles triplets that allowed the parallelism (by 5 degrees) between the [110] direction and the drawing direction: three loops were launched to cover the three Euler angles every 1 degree form 0 to 360 degrees, if the parallelism was verified with one triplet, the latter would be saved. Upon defining the orientation for a grain, a random selection among the obtained triplets was carried out if the grain was associated with the texture. Otherwise, a random orientation was retained to have the 30% of the grains free of the texture. A representative orientation distribution for numerical RST plate is highlighted in Fig. 16. The green and blue axes denote the drawing direction and the perpendicular direction, respectively. The RD inverse pole figure gives insight to the texture with the stereographic projections localized by the [110] top. However, the TD inverse pole figure reveals a scattered projection pattern, which means that there is no privileged crystallographic axis in the perpendicular direction.

For uniformity, the numerical assessment was also carried out with the beam theory applied to the numerical force-deflection curve. All the obtained results were then corrected with the determined relative error.

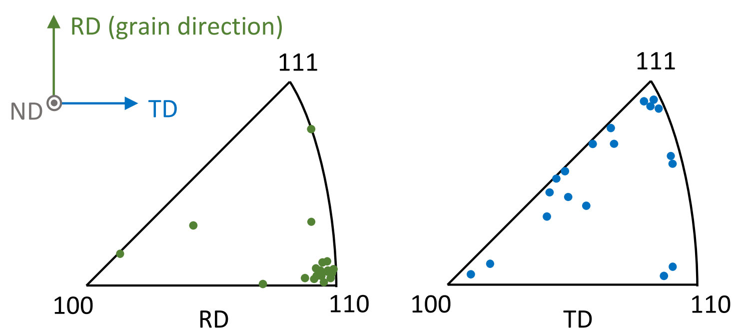

Figure 16: Artificial texture of RST plates for the stiffness characterization using the FE model: inverse pole figure for the grain direction (RD) and inverse pole figure for the perpendicular direction (TD)

5. Results

5.1. Characterization of Young's modulus with relative error correction

Three representative experimental stress-strain curves for the lower surface (in tension) in the inner span region are displayed and compared with three numerical ones in Fig. 17. The experimental and numerical results match well till the fracture. The sharp drop is characteristic of the brittle nature of the material. It can be noted that the two curves for the MCSi plate and the RST plate with grains parallel to the punch rollers possess very close slopes, which indicates a similar Young's modulus. However, the slope of the curve for the RST plate in the other loading direction is more important, which reveals a higher rigidity.

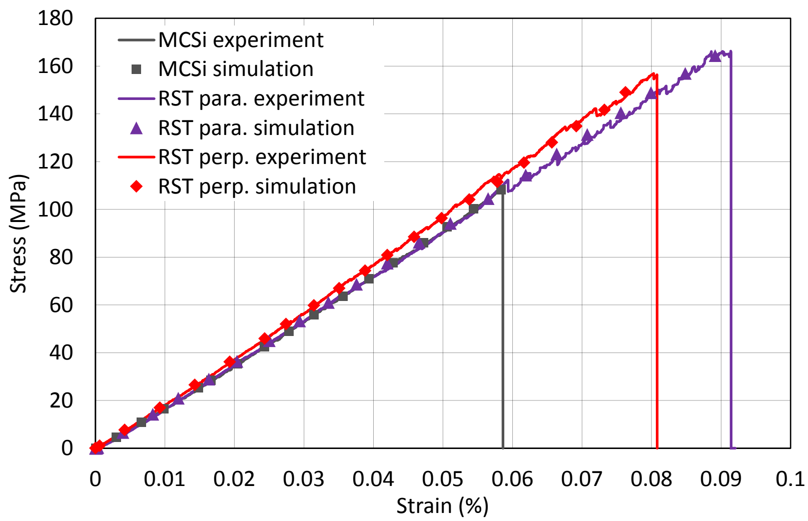

Figure 17: Representative experimental and numerical stress-strain curves for MCSi and RST plates

- Elasticity of MCSi plates

  From the experimental characterization combined with the correction based on the preliminary FE analysis, the equivalent Young's modulus of the MCSi silicon wafer when averaged as homogeneous and isotropic material is 166±5 GPa. From full FE simulation, the equivalent Young's modulus is assessed as 163±2 GPa, which is in good agreement with experiments.

- Elasticity of RST plates

  The experimental characterization gives as equivalent Young's modulus 172±4 GPa when grains are elongated along the longitudinal direction and 163±6 GPa when grains are oriented in the perpendicular direction. The corresponding simulations result in an equivalent Young's modulus of 171±3 GPa and 164±3 GPa in the two directions, which match well the experimental results. The difference between the two directions in both experimental and numerical assessments reveal an anisotropy of the RST plates, which correlates with the preliminary EBSD measurements.

5.2. *Fracture investigations*

5.2.1. *On the fracture mode*

- MCSi failure mode

Figure 18 presents two successive images of the fracture of a MCSi plate, the third one being a copy of the second one which underlines the longest crack pass. Note that, conversely to Fig. 7, the central rollers are located at the left and right sides of each photo (i.e. vertical), which is also the bending axis. Thus the tensile direction on the observed side is horizontal. The cracks are easily observed thanks to the apparition of gray broken lines. It can be seen in Fig. 18 that the cracks remain straight in each grain but the propagation direction changes when they enter into a new grain. In the largest grain (top) many parallel cracks are observed. No crack is observed at the grain boundaries. This crack pattern indicates that the fracture is trans-granular and takes place on some specific planes rather than the plane perpendicular to the maximum tensile stress. [1]

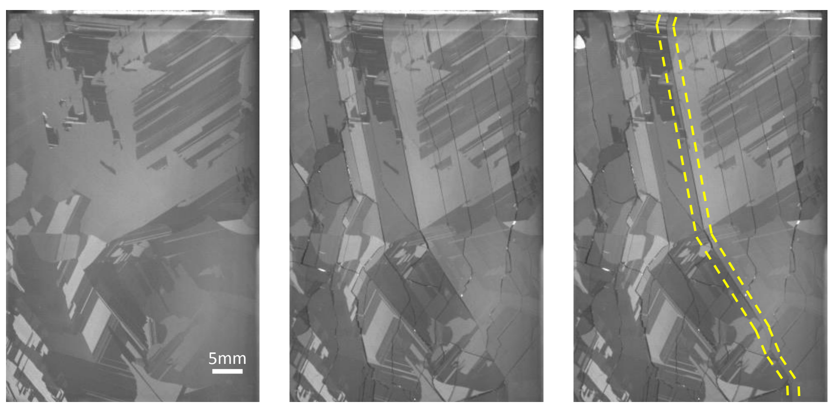

Figure 18: MCSi plate before (left) and after (right) cracking.

- RST failure mode

[1]Note that a video animation of the fracture of a MCSi plate during a tensile test is attached as supplementary material. The FE model has been build with Abaqus v6.13 using X-FEM, with C3D8R elements. A small pre-crack is visible on the top left side of the plate, from where the main crack will initiate and propagate.

In the case where the grains are perpendicular to the tension direction, the cracks are quite straight and likely cross through the whole plate without remarkable direction change, as shown in Fig. 19. The conclusion for the fracture mode is not straightforward to the naked eye since the roughness and the multitude of twins prevent from properly identifying the grain boundaries. However, by fractography, the straight long crack facies can be observed and a representative part is shown in Fig. 20. One can observe that the fracture surface is very smooth, while the grain boundaries present mostly curved shapes, as shown in Fig. 5. Thus, it is believed that the fracture takes place on a cleavage plane rather than along a grain boundary.

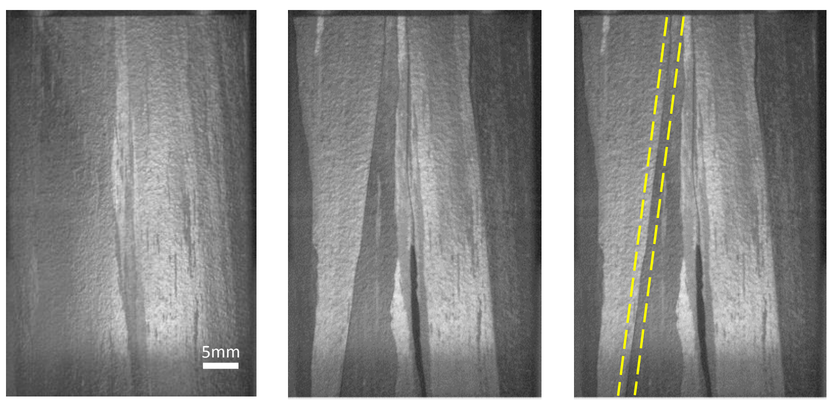

Figure 19: RST plate before (left) and after (right) cracking with grains perpendicular to the tension direction.

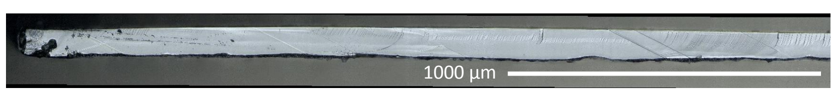

Figure 20: Facies of RST plate crack with grains perpendicular to the tension direction

Regarding the load case where the elongated grains are parallel to the tension direction, one can observe in Fig. 21 that each crack passes through the plate with multiple direction changes. Moreover, all the crack paths seem to be aligned with each other. The fracture mode is certainly trans-granular and likely based on cleavage planes. Little change in the crack propagation direction also emphasizes the fact the grain orientations are very close, so the global behavior should be anisotropic.

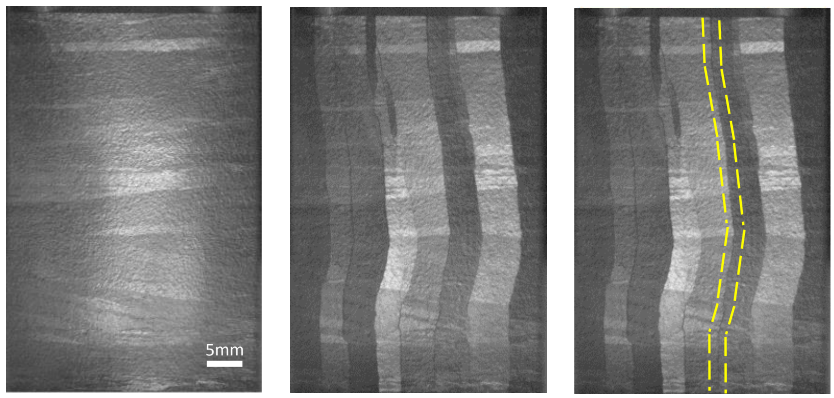

Figure 21: RST plate before (left) and after (right) cracking with grains parallel to the tension direction.

5.2.2. *On the fracture origin*

- MCSi failure source

  As illustrated in Fig. 22, the analysis of consecutive images enables the identification of the first cracks that is framed in the right image. This image comes from the subtraction of the two left photos that correspond to the last image before and the first image after the cracking.

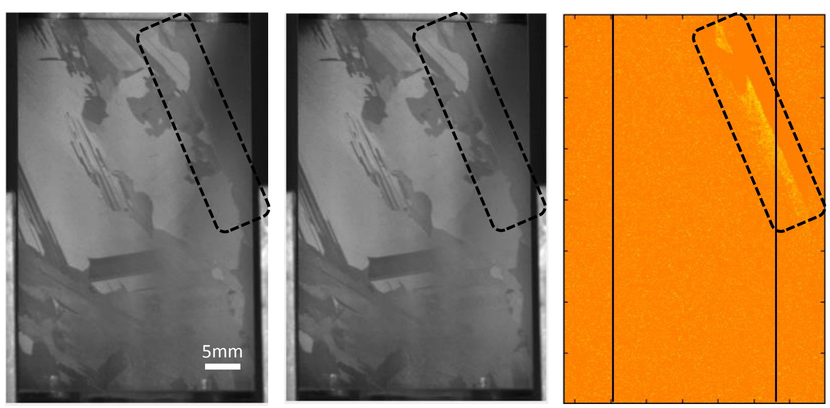

Figure 22: First cracks marked in two consecutive images for MCSi plate with (left) the last image before cracking and (center) the first image after cracking. Why these are the first cracks is coming from analysis by image subtraction (right). The two black vertical lines in the right image reveal the punch rollers' positions.

The fractography brings us to the fracture origin located facies shown in Fig. 23. The Wallner lines are not noticeable. Meanwhile, the surface perturbations help to identify the tensile and compression sides as well as the crack propagation direction, which ultimately enables us to locate the fracture origin, as pointed out by the arrow. To enhance the readability, Fig. 24 shows the further propagation direction at the end of the same crack as in Fig. 23. In this specific example, the initiation point is located at the edge. Basically it has been found that most crack initiation sites are located at the edge or at a point less than 200μm from the edge. It can be concluded that, for MCSi plates, fracture mainly initiates on the edges of the wafer on defects assumed to be caused by laser cutting.

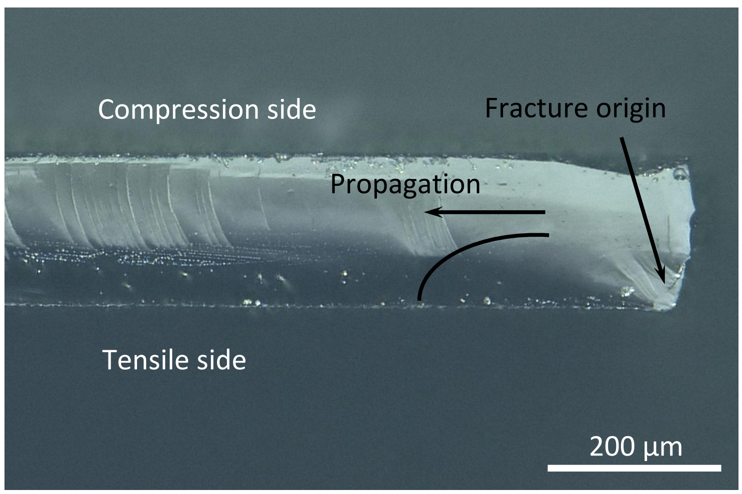

Figure 23: Fracture facies pointing out the crack initiation site for a MCSi plate

- RST failure source

The same process is used to identify the first crack created during the bending tests with RST plates. An example is given in Fig. 25, where the first crack is framed in the right image. Here the punch rollers are parallel to the drawing direction i.e. parallel to the grains (vertical).

One fractography showing the corresponding fracture facies is presented in Fig. 26. Once again, the tensile and compression sides of the wafer and the propa-

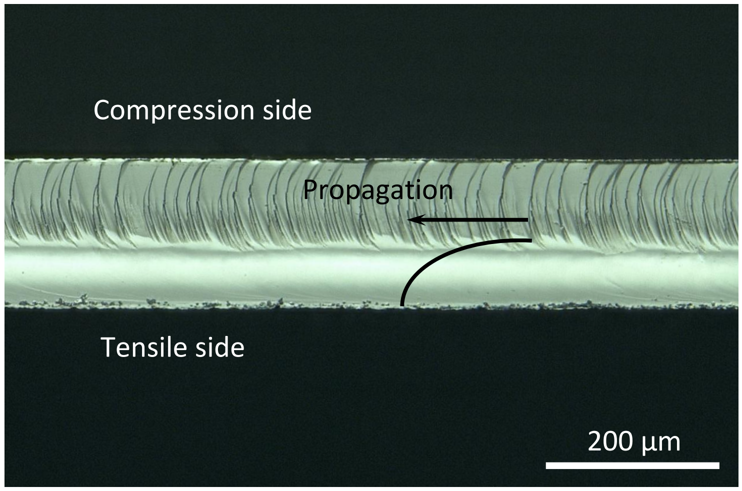

Figure 24: Fracture facies on the same crack as in Fig. 23 pointing out further propagation direction

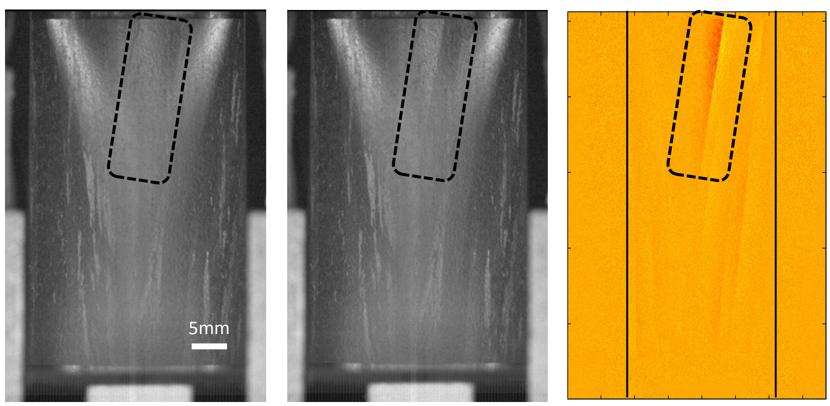

Figure 25: First crack marked in two consecutive images for RST plate with (left) the last image before cracking and (center and right) the first image after cracking. The two black vertical lines in the right image reveal the punch rollers' positions.

gation directions are determined thanks to the presence of surface perturbations (marked by the black arrows). The crack origin is easily identified and spotted by the black arrow. Figure 27 addresses further propagation direction on the same crack as in Fig. 26 for a better substantiation. In this test, the fracture initiated on a large defect, 250µm far from the edge of the plate. Several other RST bending tests have been analyzed this way and none of the observed fractures seems to have been initiated from a thickness reduction, even if the local variation may reach 20%, as shown in Fig. 28. No precipitate or inclusion has been identified as crack source, neither. The passage through some inclusion like defects is observed and presented in Fig. 29. To conclude for RST plates, the fracture is believed to initiate almost always from defects close to the edges, probably induced by the laser cutting, as for MCSi ones.

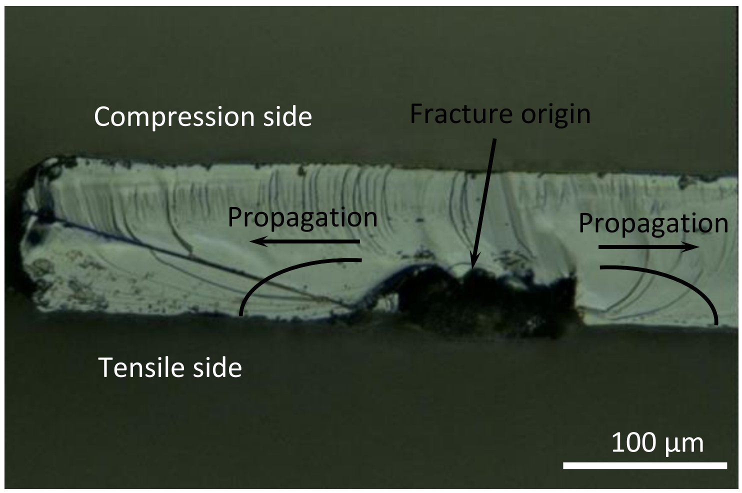

Figure 26: Crack facies pointing out the initiation site in a RST plate

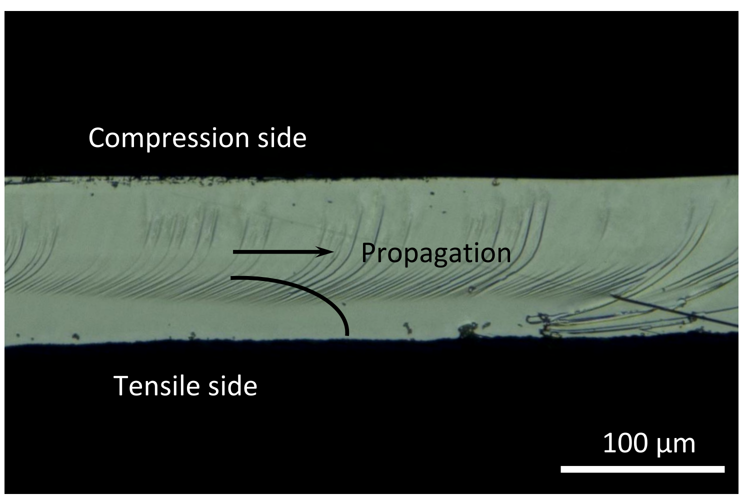

Figure 27: Fracture facies on the same crack as in Fig. 26 pointing out further propagation direction

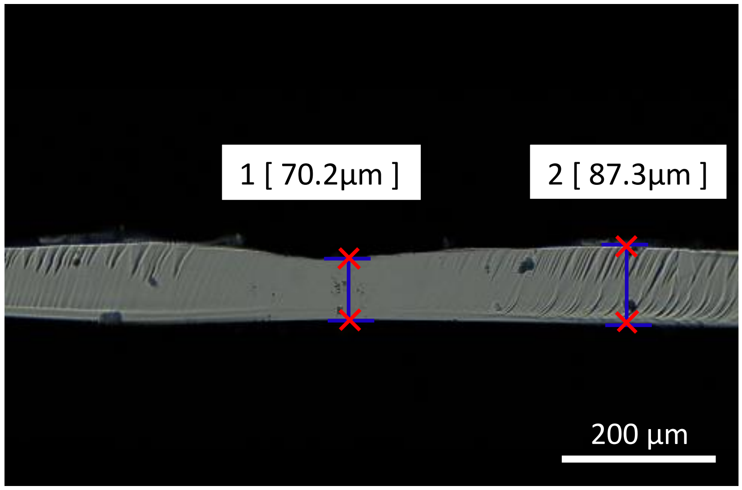

Figure 28: Significant variation of thickness of a RST plate

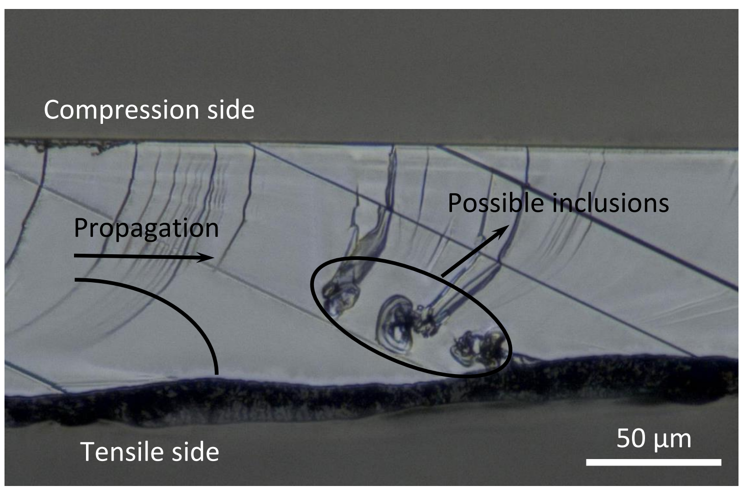

Figure 29: Possible inclusions in a RST plate .

For RST plates in which the drawing direction is perpendicular to the punch rollers, the fracture facies is much more complicated. An example of fractography is presented in Fig. 30, where the crack facies highlights unceasing changes of the cleavage planes. The latter are of very small widths, typically in the order of a few tens of µm. Therefore, no straight conclusion can be made here regarding the initiation point. These so frequent changes in cleavage planes indicate that there are intensive twining in this kind of silicon wafers.

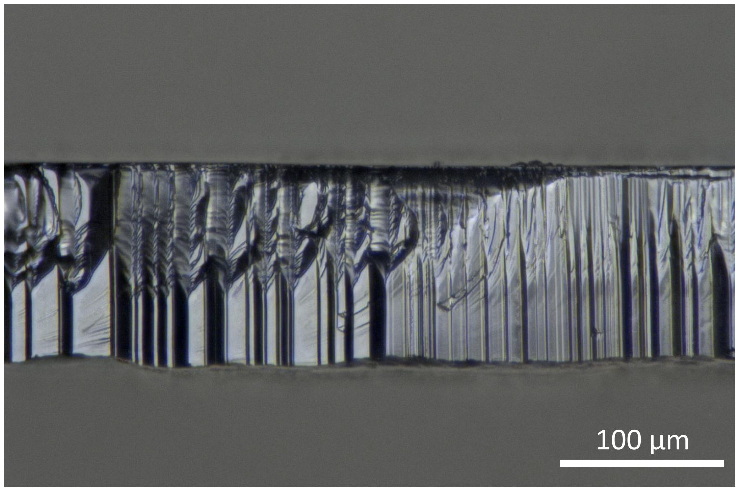

Figure 30: Crack facies of a RST plate with grains elongated along the direction perpendicular to the punch rollers

5.2.3. Weibull distribution analysis

The Weibull distributions plotted from our tested samples are shown in Fig. 31, and the corresponding parameters are listed in Table 2. RST perp. and RST para. denote the tensile stress direction perpendicular and parallel to the RST grains, respectively. It has been noticed that the fracture initiates from the laser cut edge for MCSi plates and RST plates with grains parallel to the punch rollers. Thus, the Weibull distribution evaluates particularly the laser cutting induced defects.

Table 2: Weibull parameters with 90% confidence intervals for MCSi and RST plates

Specimen	**Test quantity**	**Char. Fracture stress** σ_θ [MPa]	**Weibull Modulus** m [-]
MCSi	21	106 (100...113)	6.3 (4.9...8.7)
RST perp.	30	152 (144...161)	5.8 (4.6...7.4)
RST para.	30	159 (148...166)	6.1 (5.1...9.6)

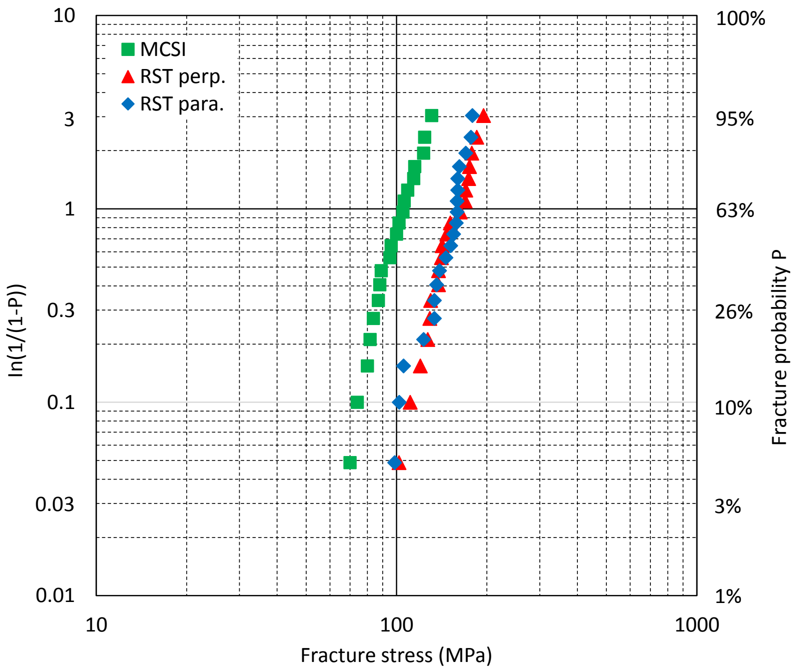

Figure 31: Weibull distributions of both MCSi plates and RST plates in the two loading configurations

From the Weibull parameters, one can see that the strength of the MCSi plates is lower than that of the RST plates. The latter possess almost the same fracture stress in the two considered directions. Concerning the Weibull moduli (slopes), the three cases hold all a value of about 6. This reveals that the fracture may have the same origin for the studied plates: defects due to manufacturing process especially edge laser cutting.

6. Discussion

6.1. Identification of the Young's modulus

For a thin brittle material, the 4-point bending test is a very appropriate characterization method. Yet, for high accuracy assessment, the beam theory owns some limitations due to strong hypotheses such as homogeneity, isotropy, linear elasticity, perfect contact condition, and no Poisson's ratio effect.

In our study, the two kinds of silicon plates possess different micro-structures, with RST kind owning a specific texture due to the manufacturing process. The recall of existing works and the elasticity of mono-crystalline silicon allowed to highlight a reasonable range for the stiffness of multi-crystalline silicon. The FE analysis has been employed to improve the accuracy and to enhance the reliability of the characterization. It should be noted that the EBSD analysis for plates as large as $50\times50 mm^2$ is still challenging with most SEM. Therefore we have chosen to perform numerical simulations with a simplified microstructure, as representative as possible of the tested samples.

With the correction procedure used to analyze the experimental data we have found that the Young's modulus of MCSi plates is close to 165 GPa, which is coherent with the literature. In the other hand simulations performed with a stochastic distribution of grain orientation have been also found in very good agreement with measurements. The FE simulations result in a very similar value (163 GPa), which justifies the aleatory grain orientations, as mentioned in Section 3.1. Regarding RST plates, the preliminary EBSD measurements show a specific micro-structural texture with the [110] axis essentially aligned along the drawing direction. The distinction of loading direction with respect to the elongated grains leads to two different equivalent rigidities. The corresponding numerical assessment matches very well the experimental characterization when the texture effect is taken into account. It is quite remarkable to see that the characterized Young's modulus in the drawing direction, 172 GPa and 171 GPa from the experimental and numerical assessments, is comparable to that in the [110] axis, 169 GPa.

6.2. Fracture investigation

The fracture mode for crystalline silicon is an interesting issue. The specific cleavage planes for a mono-crystal are well-known. For multi-crystalline silicon, trans-granular, inter-granular modes were both addressed in the literature. Meanwhile, it should be noted that the works based on the inter-granular fracture did not have any experimental support.

Concerning the silicon plates studied in this work, the failure mode was investigated by high speed imaging technique and fractography when necessary. For MCSi plates, it is found that the cracks never overlap the grain boundaries, conversely they follow cleavage planes as in a mono-crystal of silicon. Further works should be performed to identify properly the cleavage planes. On the facies where are located the fracture initiation spots, one can observe the specific surface perturbations (see Figs. 23 and 24). These perturbations have only been reported to be present on the {111} crack facies, as presented in Sherman (2009) and revealed in our study on a mono-crystal silicon plate (see Fig. 9). This finding indicates that the crack initiates on one of the {111} planes. Regarding the RST plates, when the tensile stress direction is perpendicular to the grains, it is not obvious a priori to state if the cracks follow the grain boundaries or a cleveage plane within a silicon crystal. However based on a fractography analysis, it has been observed that the grain boundaries are mostly curved while the cracks follow a plane path (see Fig. 20). Consequently it can be concluded that the plates crack on some cleavage planes. Moreover, the fractography on the first crack reveals also the presence of perturbations as expected in the {111} surface (see Figs. 26 and 27). These perturbations highlight that the crack initiates on one of the {111} planes as for MCSi specimens. For RST plates in the other configuration, i.e. when the grain boundaries are almost parallel to the tensile stress, the cracks propagate perpendicular to the grains. Therefore it is clear here that the crack path does not follow grain boundaries. It has been also observed that each crack deviates when entering into a new grain. In addition many parallel cracks can be seen in each grain, again following a certain cleavage plane. One may so conclude that the crack propagation mode in solar grade silicon, for mono-crystal or MCSi or RST, is transgranular and that the crack path follows one of the cleavage planes as {111} or {110}.

The crack path is energetically chosen to release the store deformation energy. Mono-crystal silicon fractures mostly in low energy planes as {111} and {110}, as mentioned in the introduction. For MCSi the literature outlines two possible crack paths, either one of the cleavage planes or the grain boundaries. In our experiments, based on the fracture of more than 100 silicon plates, no inter-granular fracture event has been observed. Indeed, at a grain boundary, the atomic arrangements are complex due to the disorientation of the atom arrangements and the accumulation of dislocations (Seager, 1985). Interestingly, these immobile dislocations can perturb the propagation of the crack and generate a local deflection in the Si crystal, as reported by Sherman and Be’ery (2004). The crossing of a dislocation is not energetically favorable. Thus, when the crack reaches a grain boundary, the crack front may be trapped in the disarranged atomic region where many dislocations are accumulated, so that it deviates toward one of the lowest energy planes in the neighboring grain to propagate further.

As mentioned in the introduction, the identification of the fracture origin in silicon PV plates has been investigated by Klute et al. (2014). These authors relied only on fractography to find out the fracture cause of silicon wafer, and the observations incriminated wire sawing induced micro-cracks. However, this study was limited to mono-crystalline silicon wafers in the framework of 3-point bending tests. It has been concluded that the cracks follow one of the cleavage planes. In addition it is worthy to mention that the fracture of a rectangular plate made in a single crystal of Si under 3-point bending test leads to a few large fragments whereas many small fragments are produced when a MCSi or a RST plate fractures with 4-point bending (see Fig. 18). It means a lot of work to perform the fractography analysis in order to identify the potential initiation site. This difficulty has been overcame by the use of a high speed imaging technique to detect and locate the first crack, limiting the fractography analysis to this first crack. With these two correlated methods, it is found that the fracture initiates from the plate edges on laser cutting induced defects for MCSi plates and the RST ones when the tensile stress is perpendicular to the grains (see Figs. 23 and 26). Although it is difficult to determine the fracture origin in RST plates undergoing the tensile stress in the grain direction, the Weibull distributions indicate that the fracture origin should be the same as in the other loading configuration.

Finally the Weibull distribution analysis has shown that a lower fracture stress is found for MCSi plates compared to the RST ones, i.e. 106 MPa against 152−159 MPa. It should be noticed that the flexural strength of a brittle material is dependent on both the fracture toughness and the defect size (ASTM C 1161-02c). For crystalline silicon, the toughness slightly varies from one cleavage plane to the other since $K_{IC(110)}/K_{IC(111)} = 1.1$ as reported by Li et al. (2005). Thus, the key factor for the failure strength is the severity of the defects. Since MCSi plates are thicker than the RST ones, they need more laser energy to be cut which indeed produces more and more severe defects. This explains the lower strength found for MCSi plates than for RST plates. The Weibull slope is close to 6 for the three sets of tested Si plates. To compare with the wire sawing induced fracture root, 9 has been obtained in (Popovich et al., 2011) and 11.3 in (Funke et al., 2004) for multi-crystalline silicon wafers, while a much higher value of 26 has been reported in (Klute et al., 2014) for mono-crystalline silicon wafers. The mono-crystal undergoes the defects with less scattered sizes since it is free of the influence of grain orientation, which should affect the interaction between the cutting particles and the crystal from one grain to another due to the anisotropic fracture behavior. Concerning the silicon multi-crystal, the laser cutting results in a slightly larger but comparable dispersion of the strength with respect to that induced by the wire sawing. This is probably due to the fact that the laser defect is affected by many factors in the cutting process such as the laser energy, the cutting velocity and the thickness of the plate.

7. Conclusion

The objectives of this study were to characterize the rigidity and analyze the fracture behavior of solar grade multi-crystalline silicon plates. The studied specimens possess two different micro-structures corresponding to two different manufacturing processes. For MCSi specimens, the grain orientation was considered as aleatory, while for RST ones, a specific texture was revealed by EBSD measurements which showed that the [110] direction of the grains was mainly parallel to the drawing direction. Regarding the stiffness characterization from 4 point-bending tests, the beam theory was applied based on the force-deflection curve. Meanwhile a FE model was elaborated to quantify the relative error inherent to the beam theory when applied to the bending of a thin plate and characterize the Young's modulus from a numerical point of view. For fracture investigation, a high speed imaging technique and fractography were carried out to identify the fracture mode and its origin. A Weibull analysis has then be performed and both the mean stress and the Weibull slope have been identified. The main conclusions are the following:

(1) The MCSi plates possess a mean Young's modulus of 166 GPa. This value is comparable with data for poly-crystalline silicon when it contains micro range grains (160 GPa) and the numerical assessment that considers similar grain size but aleatory grain orientation (163 GPa).

(2) The RST plates own two different Young's moduli depending on the bending direction relative to the grain elongated orientation. In the grain direction, the characterization gives 172 GPa which is similar to the rigidity in the [110] crystallographic axis (169 GPa); in the perpendicular direction, the assessment results in 163 GPa which is close to the Young's modulus of poly-crystalline silicon. For FE results, the consideration of the texture allows to match the experimental assessment with comparable rigidities 171 GPa in the grain direction and 164 GPa in the perpendicular direction .

(3) Both kinds of plates fracture in trans-granular mode. The first crack facies is revealed to be one of the {111} planes. The crack path deviates at the grain boundary when it skips from one grain to the next one. Straight cracks have been also observed in RST plates when the bending direction is parallel to the direction the grains are elongated (i.e. when the tensile stress is perpendicular to the grains).

(4) The pre-existing defects on the plate edges due to the laser cutting have been identified as the fracture origin for both kinds of plates. These defects lead to a lower mechanical strength for MCSi plates (106 MPa) compared to the one for RST plates (152 – 159 MPa). It should be also emphasized that these fracture stresses are at least one order of magnitude lower than the one observed for a mono-crystal of Si (5 to 7 GPa). The Weibull modulus of 6 obtained here experimentally tends to show a limited scatter in the distribution of laser induced defects.

Outlook: further development and investigation will address the failure modes of silicon cells embedded into a PV module. In that case, the critical fracture sources might differ substantially from what is observed for silicon wafer. For instance, critical sources for cracks might also be soldered points between the busbars and the silicon cell as well as residual stress due to lamination (thermal) process.

Acknowledgment: The authors would like to thank Prof. O. Hubert from LMT Cachan for his kind help for the EBSD characterization. We also thank Elsa Tupin, Fabrice de Moro and Christian Bellouet from Solarforce for precious exchanges about this work, carried out in the framework of the DEMOS FUI project. The authors also thank the French research agency ANR for partial funding through the DURASOL Equipex project.

References

Alexander, H., Haasen, P., 1969. Dislocations and plastic flow in the diamond structure. Solide State Physics 22, 27–158.

ASTM C 1161-02c, . Standard test method for flexural strength of advance ceramics at ambient temperature .

Bourgeois, C., Steinsland, E., Blanc, N., de N.F. Rooij, 1997. Design of resonators for the determination of the temperature coefficients of elastic constants of monocrystalline silicon, in: Frequency Control Symposium, 1997., Proceedings of the 1997 IEEE International, pp. 791–799.

Brede, M., 1993. The brittle-to-ductile transition in silicon. Acta Metallurgica et Materialia 41, 211–228.

Brodie, R., Bahr, D.F., 2003. Fracture of polycrystalline silicon. Materials Science & Engineering, A 351, 166–173.

Bruneau, A.A., Pratt, P.L., 1962. The bending deformation of magnesium oxide. Philosophical Magazine 7, 1871–1885.

Chen, J., Qiao, Y., 2007. Secondary cracking at grain boundaries in silicon thin films. Scripta Materialia 57, 1069–1072.

Coffman, V.R., James, P.S., 2008. Grain boundary energies and cohesive strength as a function of geometry. Physical Review B 77, 144111.

De Moro, F., Focsa, A., Derbouz, K., Slaoui, A., Auriac, N., Lignier, H., Keller, P., 2012. Multicrystalline silicon solar cells from rst ribbon process. Physica Status Solidi C 9, 2092–2096.

Ebrahimi, F., Kalwani, L., 1999. Fracture anisotropy in silicon single crystal. Materials Science and Engineering: A 268, 116–126.

Frechette, V.D., 1990. Failure Analysis of Brittle Materials: Advances in Ceramics. American Ceramic Society.

Funke, C., Kullig, E., Kuna, M., Möller, H.J., 2004. Biaxial fracture test of silicon wafers. Advanced Engineering Materials 6, 594–598.

Hall, J.J., 1967. Electronic effects in the elastic constants of n-type silicon. Physical Review 161, 756–761.

Hauch, J.A., Holland, D., Marder, M.P., Swinney, H.L., 1999. Dynamic fracture in single crystal silicon. Physical Review Letters 82, 3823–3826.

Holland, D., Marder, M., 1998. Ideal brittle fracture of silicon studied with molecular dynamics. Physical Review Letters 80, 746–749.

Hopcroft, M., Nix, W., Kenny, T., 2010. What is the young's modulus of silicon. Journal of Microelectromechanical Systems 19, 229–238.

Hull, R., 1999. Properties of Crystalline silicon. Institution of Electrical Engineers.

Infuso, A., Corrado, M., Paggi, M., 2014. Image analysis of polycrystalline solar cells and modelling of intergranular and transgranular cracking. Journal of the European Ceramic Society 34, 2713–2722.

Kaule, F., Wang, W., Schoenfelder, S., 2014. Modeling and testing the mechanical strength of solar cells. Solar Energy Materials and Solar Cells 120, Part A, 441–447.

Klute, C., Kaule, F., Schoenfelder, S., 2014. Breakage root cause analysis in as-cut monocrystalline silicon wafers, in: 29th European Photovoltaic Solar Energy Conference and Exhibition.

Kohler, D., Zuschlag, A., Hahn, G., 2014. On the origin and formation of large defect clusters in multicrystalline silicon solar cells. Solar Energy Materials & Solar Cells 120, 275–281.

Köntges, M., Kunze, I., Kajari-Schröder, S., Breitenmoser, X., Bjørneklett, B., 2011. The risk of power loss in crystalline silicon based photovoltaic modules due to micro-cracks. Solar Energy Materials & Solar Cells 95, 1131–1137.

Li, X.P., Kasai, T., Nakao, S., Ando, T., Shikida, M., Sato, K., Tanaka, H., 2005. Anisotropy in fracture of single crystal silicon film characterized under uniaxial tensile condition. Sensors and Actuators, A: Physical 117, 143–150.

Masolin, A., Bouchard, P.O., Martini, R., Bernacki, M., 2012. Thermo-mechanical and fracture properties in single-crystal silicon. Journal of Materials Science 48, 979–988.

Möller, H., Funke, C., Rinio, M., Scholz, S., 2005. Multicrystalline silicon for solar cells. Thin Solid Films 487, 179–187.

Paggi, M., Berardone, I., Infuso, A., Corrado, M., 2014. Fatigue degradation and electric recovery in silicon solar cells embedded in photovoltaic modules. Scientific Reports 4, 4506–.

Paggi, M., Corrado, M., Berardone, I., 2016. A global/local approach for the prediction of the electric response of cracked solar cells in photovoltaic modules under the action of mechanical loads. Engineering Fracture Mechanics , In Press-doi:http://dx.doi.org/10.1016/j.engfracmech.2016.01.018.

Pérez, R., Gumbsch, P., 2000. An ab initio study of the cleavage anisotropy in silicon. Acta Materialia 48, 4517–4530.

Popovich, V., Yunus, A., Janssen, M., Richardson, I., Bennett, I., 2011. Effect of silicon solar cell processing parameters and crystallinity on mechanical strength. Solar Energy Materials & Solar Cells 95, 97–100.

Qiao, Y., Chen, J., 2008. Resistance of through-thickness grain boundaries to cleavage cracking in silicon thin films. Scripta Materialia 59, 251–254.

Reinoso, J., Paggi, M., Areias, P., 2016. A finite element framework for the interplay between delamination and buckling of rubber-like bi-material systems and stretchable electronics. Journal of the European Ceramic Society 36, 2371–2382.

Samuels, J., Roberts, S.G., 1989. The brittle-ductile transition in silicon. i. experiments. Proceedings of the Royal Society of London. Series A, Mathematical and Physical Sciences 421, 1–23.

Sander, M., Dietrich, S., Pander, M., Ebert, M., Bagdahn, J., 2013. Systematic investigation of cracks in encapsulated solar cells after mechanical loading. Solar Energy Materials and Solar Cells 111, 82–89.

Seager, C.H., 1985. Grain boundaries in polycrystalline silicon. Annual Review of Materials Science. 15, 271–302.

Sharpe Jr, W.N., 2001. Mechanical properties of mems materials, in: Semiconductor Device Research Symposium, 2001 International, pp. 416–417.

Sherman, D., 2003. Hackle or textured mirror? analysis of surface perturbation in single crystal silicon. Journal of Materials Science 38, 783–788.

Sherman, D., 2009. Fractography of dynamic crack propagation in silicon crystal. Key Engineering Materials 409, 55–64.

Sherman, D., Be'ery, I., 2003. The shape and the energies of a dynamically propagating crack under bending. Journal of Materials Research 18, 2379–2386.

Sherman, D., Be'ery, I., 2004. Dislocations deflect and perturb dynamically propagating cracks. Physical Review Letters 93, 265501.

Søiland, A.K., Øvrelid, E.J., Engh, T.A., Lohne, O., Tuset, J.K., Gjerstad, Ø., 2004. Sic and si3n4 inclusions in multicrystalline silicon ingots. Materials Science in Semiconductor Processing 7, 39–43.

Sudani, N., Venkatakrishnan, K., Tan, B., 2009. Laser singulation of thin wafer: Die strength and surface roughness analysis of 80m silicon dice. Optics and Lasers in Engineering 47, 850–854.

Weibull, W., 1951. A statistical distribution function of wide applicability. Journal of Applied Physics 18, 293–297.

Wu, H., Melkote, S.N., 2013. Effect of crystal defects on mechanical properties relevant to cutting of multicrystalline solar silicon. Materials Science in Semiconductor Processing 16, 1416–1421.

Yang, Z.P., Zhang, H.P., Mader, M., 2008. Dynamics of static friction between steel and silicon. Proceedings of the National Academy of Sciences of the United States of America 105, 13264–13268.

Appendix A. Thickness profiles for MCSi and RST plates

The assessment of the thickness variation was performed with the optical microscope Keyence VHX-2000. The measurements covered the whole edge of the specimen with a step of 0.5 mm. The figure below shows the thickness profiles for a typical MCSi plate and two typical RST plates for the grain direction as well as the perpendicular direction, with averages and standard deviations of 170µm, 96µm, 89µm, and 2µm, 4µm, 4µm, respectively.

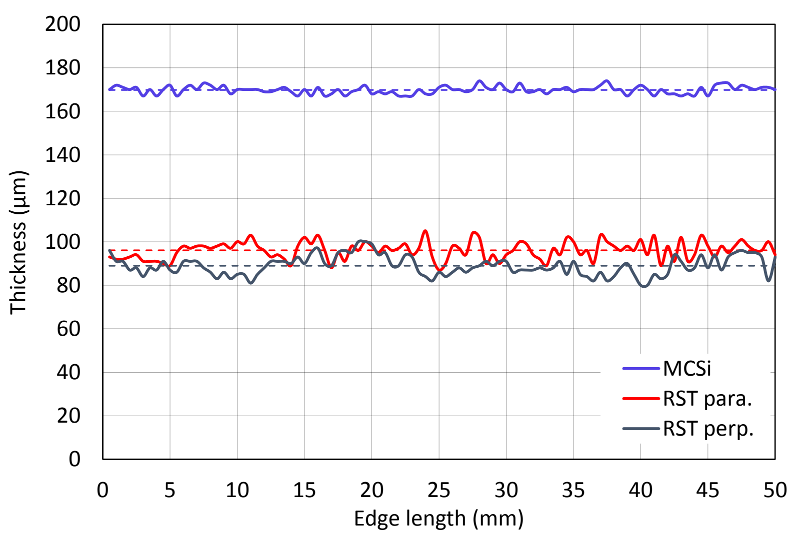

The dotted lines denote the averaged thickness calculated with the 100 measurement data. It can be noted that the RST plates undergo more important thickness variation than the MCSi plates. Meanwhile, the thicknesses for both kinds are not monotonously increasing or decreasing from one side to the other along the edge. This enables us to use the averaged thickness of the specimen in the characterization.